Toward Image Data-Driven Predictive Modeling for Guiding Thermal Ablative Therapy

Jarrod A. Collins, Jon S. Heiselman, Logan W. Clements, Jared A. Weis, Daniel B. Brown, and Michael I. Miga, *Member, IEEE*

Abstract*—*Objective: **Accurate prospective modeling of microwave ablation (MWA) procedures can provide powerful planning and navigational information to physicians. However, patient-specific tissue properties are generally unavailable and can vary based on factors such as relative perfusion and state of disease. Therefore, a need exists for modeling frameworks that account for variations in tissue properties.** ***Methods:*** **In this study, we establish an inverse modeling approach to reconstruct a set of tissue properties that best fit the model-predicted and observed ablation zone extents in a series of phantoms of varying fat content. We then create a model of these tissue properties as a function of fat content and perform a comprehensive leave-one-out evaluation of the predictive property model. Furthermore, we validate the inverse-model predictions in a separate series of phantoms that include co-recorded temperature data.** ***Results:*** **This model-based approach yielded thermal profiles in close agreement with experimental measurements in the series of validation phantoms (average root-mean-square error of 4.8 °C). The model-predicted ablation zones showed compelling overlap with observed ablations in both the series of validation phantoms (93.4 ± 2.2%) and the leave-one-out cross validation study (86.6 ± 5.3%). These results demonstrate an average improvement of 17.3% in predicted ablation zone overlap when comparing the presented property-model to properties derived from phantom component volume fractions.** ***Conclusion:*** **These results demonstrate accurate model-predicted ablation estimates based on image-driven determination of tissue properties.** ***Significance:*** **The work demonstrates, as a proof-of-concept, that physical modeling parameters can be linked with quantitative medical imaging to improve the utility of predictive procedural modeling for MWA.**

***Index Terms*—Microwave ablation, finite element, optimization, tissue, liver, dielectric, thermal, therapeutic planning, modeling.**

Manuscript received June 25, 2019; accepted September 2, 2019. Date of publication September 5, 2019; date of current version May 20, 2020. This work was supported by the National Institutes of Health under Award R01CA162477 from the National Cancer Institute and Award T32EB021937 from the National Institute of Biomedical Imaging and Bioengineering. *(Corresponding author: Michael I. Miga.)*

J. A. Collins, J. S. Heiselman, and L. W. Clements are with the Department of Biomedical Engineering, Vanderbilt University.

J. A. Weis is with the Department of Biomedical Engineering, Wake Forest School of Medicine.

D. B. Brown is with the Department of Radiology and Radiological Sciences, Vanderbilt University Medical Center.

M. I. Miga is with the Department of Biomedical Engineering, Vanderbilt University, Nashville, TN 37235 USA (e-mail: michael.i.miga@vanderbilt.edu).

Digital Object Identifier 10.1109/TBME.2019.2939686

I. Introduction

THERMAL ablation techniques have become a viable treatment approach in the management of anatomically non-resectable liver malignancies [1]–[3]. While many ablation modalities exist, microwave ablation (MWA) has had considerably increased interest for hepatic procedures in recent years over its counterparts. The most notable benefits when comparing to the main competing modality, radiofrequency ablation, are that MWA creates a large spatial extent of power distribution, can penetrate through charred tissues, and has the capacity to ablate up to and around large vessels [4]–[7].

Regarding performance, the success of a complete ablation with acceptable margins is heavily reliant on accurate guidance. Ablation procedures are often performed using image guidance to assist in probe placement, intraoperative localization of the target, and for postoperative evaluation of the resulting necrotic zone. When using traditional methods of guidance such as ultrasound and computed tomography (CT), the ability to monitor thermal lesion development throughout the procedure is significantly limited [8]. Methods using MR thermometry have generated considerable interest although challenges of MR-compatibility, availability, and considerable cost exist [9]. Patient-specific predictive modeling of ablation procedures has been proposed to improve treatment planning and provide an alternative to direct thermal monitoring [10].

For ablation procedural planning, MWA device manufacturers currently provide 2D specifications for generating expected ablation volumes given specific power and time settings. These estimates are empirically derived from ablations observed within ex vivo animal tissue. In doing so, these models ignore the influence of patient-specific anatomical variation, tissue heterogeneity, and tissue perfusion. As a result, the manufacturer specifications are often larger and more uniform than clinically observed ablations [11], [12]. Moreover, there is often no integration of these 2D predictions with the 3D patient images, placing burden on the physician to mentally reconstruct and compare complex volumes. The development of clinically accurate, patient-specific computational models of MWA procedures presents a powerful alternative to the ablation zone estimates provided by manufacturers and a lower-cost, less cumbersome alternative to interventional imaging strategies.

Computational models of MWA employ numerical methods to solve the differential equations governing electromagnetic wave propagation, power deposition, and biological heat transfer

and have been investigated within the literature for two distinct purposes: (1) assisting the optimization of ablation hardware design [13]–[17] and (2) more recently towards the eventual development of patient-specific treatment planning [18]–[22]. For clinical application, research into these approaches seeks to provide more accurate and reliable estimates of personalized procedures for the purposes of planning, guidance, and assessment. When considering the shortcomings of the manufacturer provided charts, computational models tailored to an individual could incorporate specifications for geometric, thermal, and electrical properties of the tissue. Sensitivity studies performed on models of 2.45 GHz MWA have highlighted the extensive influence that these tissue properties have on MWA models, especially the electrical properties, specific heat, and the rate of blood perfusion when present [26], [27]. Recent studies at both clinical frequencies (i.e., 915 MHz and 2.45 GHz) have incorporated tissue properties that vary as a function of temperature as derived from experimental measurements [20]–[25] or due to dynamic changes in tissue water content and blood perfusion [28]–[32]. However, an inherent shortcoming in these models is that they neglect the variation in material properties that can occur between patients. A recent study in MWA antenna design concluded that there is an overall need for more accurate and comprehensive modeling of tissue properties [17].

Presently, patient-specific thermal and electrical properties are generally unavailable in a clinical setting. As such, the various existing models of tissue properties are often derived from experimental conditions in animal tissue. Going further, there is clear variation between patients presenting with other common comorbidities such as nonalcoholic fatty liver disease (NAFLD), nonalcoholic steatohepatitis (NASH), and cirrhosis where excessive buildup of fat, inflammation, and scar tissue can occur [33]–[35]. Therefore, a need exists for modeling frameworks that account for patient-specific variations in the state of organ tissue. One possibility is to use imaging methods to non-invasively measure quantities that could be correlated to material property changes, e.g., quantification of liver fat content with MRI [36] may provide *a priori* knowledge of relevant properties. We propose that this *a priori* knowledge of organ disease state can be used to facilitate clinically-relevant advances in predictive modeling of thermal ablation. It is also important to realize that this is just one modality among many other possibilities (e.g., perfusion imaging).

In this work, we propose a novel approach to modeling microwave ablation procedures that uses quantitative medical imaging to estimate the thermal and electrical properties of tissue. The paper begins with the development of a methodology to determine thermal and electrical tissue material properties from an inverse modeling approach and reports the fidelity of those predictions within the context of temperature measurements. Once achieved, in a separate series of phantoms with varying fat content, material properties were determined via the inverse modeling approach. These reconstructed properties were then fit to a material property model as a function of phantom fat content, as measured with a clinically-relevant MRI fat quantification imaging sequence. A leave-one-out cross validation study was then performed which used the constructed material property model to estimate phantom material properties in a prospective implementation of the ablation model. The model-predicted ablation zones were then compared to their observed gross pathology counterparts for validation purposes. The material property model developed in this study specifically focused on phantom fat content because it was easily controllable and quantifiable for the purposes of this proof-of-concept study and remains clinically-relevant when looking at common patient presentations [33]–[36]. However, we note that for future work there are additional quantitative medical imaging methods that could be complimentary (e.g., microwave tomographic imaging [37]).

TABLE I
DIELECTRIC AND THERMAL PROPERTIES OF THE AGAR-ALBUMIN-FAT PHANTOM COMPONENTS AS REPORTED IN THE LITERATURE. RELEVANT VALUES REPORTED FOR 915–1000 MHz RANGE OF FREQUENCIES

	Agar-albumin Phantom		
	Agar-water gel (1.5%)	Vegetable Oil	Liquid Egg Whites
σ [S/m]	0.05 – 0.4 [38]	1.04 x10^{-5} [42]	1 [46]
ε	67 – 84 [39]	2.53 – 2.665 [43]	50.2 [46]
c [J/kg-K]	3900 [40]	1670 [44]	3414 [47]
κ [W/m-K]	0.5 – 0.55 [41]	0.155 – 0.170 [45]	0.522 [47]

II. METHODS

The objective of this study is to develop a predictive modeling framework for hepatic MWA that estimates tissue properties based on quantitative medical imaging of fat content to better account for patient-specific property variation and more accurately predict ablation outcome prior to treatment. In this work, we present a rigorous proof-of-concept in phantom to begin to determine the fidelity of such an approach for therapeutic intervention technologies. The following subsections detail the methods used to collect experimental phantom data (II.A-C), develop our MWA model (II.D-G), and experimentally validate our MWA and phantom property models (II.H-I).

A. Phantom Testing Environment

For this study, a heat-sensitive homogenous gel phantom was constructed consisting of liquid egg whites, vegetable shortening, and the remainder with agar gel. Egg whites consist of approximately 90% water and 10% dissolved protein. The denaturing of ovalbumin protein within the egg whites provides a visualization of thermal damage within the phantom. Thermal denaturation of the protein causes aggregation, leading to optical scattering. This denaturation causes the thermal lesion to be clearly visible when prepared in mock gross pathology following ablation. Vegetable shortening was used to introduce a controllable variability to the thermal and electrical properties of the phantom by altering the phantom fat content. Table I illustrates the general difference in thermal and electrical properties for vegetable shortening compared to the other phantom

components with appropriate references. The ranges of fat included within this study were chosen to represent the clinical presentation of NAFLD (i.e., 5–10% of liver weight).

To make this agar-albumin-fat phantom, 1.5 wt% agar powder (Thermo Fisher Scientific, Waltham, MA) was mixed with an appropriate volume of purified water. The solution was then heated gradually until boiling on a hot plate while being continuously stirred. After the agar gel had exceeded 60 °C, the desired amount of vegetable shortening was introduced (Crisco, The J.M. Smucker Company, Orrville, OH). Once boiled, the solution was then cooled below 55 °C with continuous stirring, at which point 50 wt% liquid egg white (Break Free Liquid Egg Whites, The Kroger Company, Cincinnati, OH) was added and mixed thoroughly for 1 minute. The mixture was then poured into the phantom mold and began to solidify once cooled below 35 °C. Note that the liquid egg white solution must be added when the temperature of the agar gel is below 60 °C to avoid prematurely denaturing the ovalbumin protein.

A cubic acrylic box with a volume of 1 L served as both the phantom mold and enclosure during ablation procedures. The lid to the enclosure incorporated a series of holes, centered 5 mm apart, along the midline of the phantom to enforce consistent placement of the ablation antenna and, if present, temperature sensors. During each experiment, the ablation and temperature sensors were positioned within the phantom using these guides and rigidly fixed in position at recorded depths.

In total, 6 agar-albumin phantoms with no fat were created for the inverse model validation study (II.H) and 15 agar-albumin-fat phantoms of varying fat content were created for the phantom material property model study (II.I).

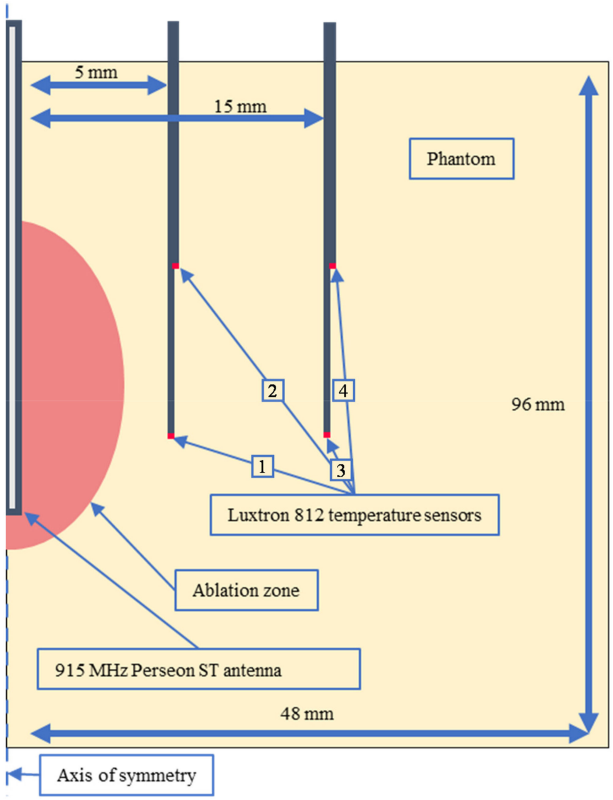

Fig. 1. Diagram of the experimental setup and model geometry for ablation with the Perseon ST microwave ablation antenna within an agar-albumin phantom.

Fig. 2. Sample mock gross pathology of ablation zone (cut along the axis of the Perseon ST antenna) following an ablation at 60 W for 15 minutes in an agar-albumin phantom.

B. Ablation Data Collection

As depicted in Fig. 1, a 915 MHz Perseon ST microwave ablation antenna was inserted into the center of each phantom to a recorded depth. For the no-fat phantoms, two two-channel Luxtron 812 (LumaSense technologies, Santa Clara, CA) fiber optic temperature sensors in conjunction with 4 STB fiberoptic probes were used to record temperatures at a rate of 2 samples per second and in the range of 0 to 120 °C. The system is reported to be accurate within ±0.5 °C and is immune to interference from radiofrequency, microwave, and electromagnetic induction [48]. Note that the relative vertical location of the antenna and thermal sensors varied slightly between ablation experiments. Continuous power of 60 W was applied for 15 minutes (MicroThermX, Perseon Medical, Salt Lake City, UT) to simulate clinical intervention. Finally, mock gross pathology was attained by sectioning the phantom along the midline of the MWA antenna. A 2D representation of the ablation zone was then segmented from a photograph (Fig. 2). Measurements of the transverse and axial extents of each ablation zone were taken from the segmented mock gross pathology.

C. MRI Fat Quantification

MRI examination of each phantom was achieved with a 3T Intera Achieva MR scanner (Philips Healthcare, Netherlands). Following ablation, a commercially available fat quantification sequence (mDixon Quant) was used to acquire fat fraction images of each of the 15 phantoms for the phantom material property model study (Philips Healthcare, Netherlands). The mDixon Quant fat quantification protocol has a reported accuracy of ±3.5% and reproducibility of ±1.4% [49]. For each

phantom, 53 slices were acquired with 3.12 mm spacing and in-plane resolution of 1.56 × 1.56 mm.

D. Computational Model

We implemented a 2D axially-symmetric finite element model using COMSOL Multiphysics (COMSOL Inc, Burlington, MA) and Matlab 2017b (The Mathworks Inc, Natick, MA) to simulate electromagnetic wave propagation and heat transfer in an agar-albumin phantom with the 915 MHz Perseon Short-tip (ST) antenna (Perseon Medical, Salt Lake City, UT). The development and absorption of electromagnetic waves radiating from the antenna within the phantom, when assuming no initial existing charge, is described by the electromagnetic wave equation.

$$\left(\nabla^2 + \omega^2 \mu \varepsilon_c\right) \vec{E} = 0 \tag{1}$$

where ω [rad/s] is the angular frequency of the electromagnetic wave, μ [H/m] is the permeability, ε_c is the complex permittivity, and $\vec{E}$ [V/m] is the electric field strength. Heat transfer and the resulting temperature history were solved using Pennes' bioheat equation.

$$\rho c \frac{\partial T}{\partial t} = \nabla \cdot \kappa \nabla T + Q - Q_p + Q_m \tag{2}$$

where ρ [kg/m^3] is mass density, c [J/kg·K] is specific heat capacity, κ [W/m·K] is thermal conductivity, T [K] is temperature, Q [W/m^3] is heat generation due to absorbed electromagnetic energy, Q_p [W/m^3] is heat loss due to perfusion, and Q_m [W/m^3] is metabolic heat generation. Metabolic heat generation (Q_m) and perfusion (Q_p) were not present within the phantom and were therefore excluded from the model. Heat generation from power deposition by the applied electric field was calculated by

$$Q = \frac{1}{2}\sigma \|E\|^2 \tag{3}$$

where σ [S/m] is the electrical conductivity. Power (60 W) was input to the model by wave excitation at a coaxial port condition at the distal end of the inner dielectric material of the ablation antenna.

E. Boundary Conditions

A first order electromagnetic scattering condition was applied to the exterior of the phantom to limit the reflection of outgoing waves by simulating a transparent boundary.

$$\vec{n} \times \left(\nabla \times \vec{E}\right) - jk\vec{n} \times \left(\vec{E} \times \vec{n}\right) = 0 \tag{4}$$

where $\vec{n}$ is the direction normal to the boundary and k is the wavenumber. Boundaries along the exterior of the phantom were set to a fixed room temperature (20 [°C]). The antenna is modeled as a conventional conductive core surrounded by dielectric material, catheter, with ring shaped slot cut on the outer conductor. Conductive material is not specifically realized but represented by the boundary condition,

$$\vec{n} \times \vec{E} = 0 \tag{5}$$

The microwave source itself is modeled as a port boundary condition which relates the field to the square root of the time average power flow in the cable and is adopted from [50]. This antenna model was consistent with observed performance, however, exact industry specifications were not available.

Saline cooling of the Perseon ST antenna was simulated as a convective heat flux condition along the inner boundary of the antenna as follows

$$\vec{n} \cdot (-\kappa \nabla T) = h \cdot (T - T_{\text{ext}}) \tag{6}$$

where $\vec{n}$ is the normal vector to the element, κ [W/m·K] is the thermal conductivity, h [W/m^2·K] is the heat transfer coefficient, T [K] is temperature, and T_{ext} is the saline temperature (20 [°C]).

F. Modeling Tissue Damage

Thermally-induced tissue damage is a function of both instantaneous temperature and thermal history. For this study, the Arrhenius damage integral was used to estimate protein denaturation as a proxy to cell death within the phantom [51]. The degree of damage in tissue experiencing hyperthermia was calculated from

$$\alpha = \int_0^t A \exp\left(-\frac{E_a}{RT\,(t)}\right) dt \tag{7}$$

where α is the degree of damage at a given time, A [1/s] is the frequency factor, E_a [J/mol] is the activation energy required to damage the phantom, R [J/mol·K] is the universal gas constant, and $T(t)$ [K] is the temperature history of the phantom. The parameters E_a (2.8819×10^5 [J/mol]) and A (1.8769×10^{41} [1/s]) are phantom dependent and were calibrated to maximize correspondence between thermal history and ablation zone contour fit in the validation phantom set. The fraction of damaged tissue was then determined by

$$\theta_d = 1 - e^{-\alpha} \tag{8}$$

G. Discretization

The ablation antenna and temperature sensor locations (when present) within the phantom were recorded in each experiment and incorporated into the model geometry as presented in Fig. 1. Four temperature sensors were used to record thermal history in each experiment of the validation phantom set with two pairs located at 5 and 15 mm transversely at varying recorded depths (observe the 4 sensor locations in Fig. 1). These locations were added within the model geometry to allow for direct comparison between model-predicted and observed temperatures at a given time. The model was discretized as a free triangular mesh with maximum element sizes of 0.15 and 1.5 mm for the antenna and phantom respectively. The wavelength of an electromagnetic wave in tissue is the primary factor for determining discretization of the computational space. For example, at 915 MHz the corresponding wavelength is 33.3 cm and therefore a maximum nodal spacing of $<$3 mm is appropriate. An implicit multifrontal massively parallel sparse direct solver (MUMPS) within COMSOL Multiphysics was used to solve both the stationary electromagnetic and transient bioheat transfer problems [50], [52]. The model was solved with a continuous input power

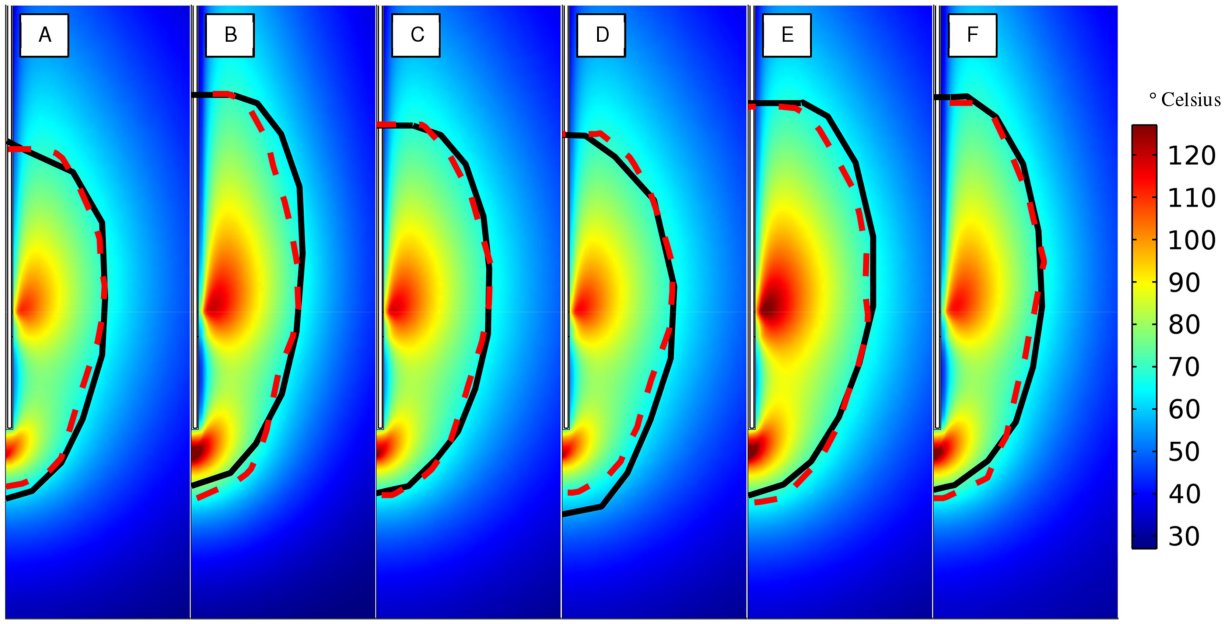

Fig. 3. Model-predicted temperature maps, observed (solid black line), and model-predicted (red dashed line) ablation zones are presented for each case (A–F) of ablation with the Perseon ST antenna at 60 W for 15 minutes within the base agar-albumin phantom used for the model validation study. The observed ablation zone contour was collected from mock gross pathology and used to drive the inverse MWA model.

of 60 W and frequency of 915 MHz at 15 s time steps to the final solution at 15 min.

H. Model Validation Study

To evaluate the fidelity of our model accuracy, a series of 6 agar-albumin phantoms with no fat were created and ablation and thermal history data were collected as described in Sections II.A–II.C. The MWA model described in Sections II.D–II.G was then employed in an inverse fashion to reconstruct a set of phantom thermal and electrical properties which best match the model-predicted ablation zone to the observed ablation zone from mock gross pathology (Fig. 3). The thermal history data collected in each case were then compared to the model-predicted temperatures to validate the accuracy of the proposed phantom property reconstruction method.

Properties defining the thermal and electrical behavior of the phantom were reconstructed by deploying the MWA model within a nonlinear optimization scheme. This inverse modeling approach iteratively selected values for a parameter set, $P = [\sigma, \kappa]$, to maximize the overlap between the observed ablation zone and the model result (as the Jaccard similarity coefficient, Eq. (9)–(10), similar to the work of [53] for predictive modeling of laser ablation. The properties allowed to vary, σ and κ, are the electrical and thermal conductivities respectively. These properties were selected for our model as they directly scale the electrical and thermal contributions to the bioheat equation (Eq. (2)–(3)). Initial values for the parameter set, as well as other properties used in the model but not reconstructed in the optimization, were estimated to be the average weighted linear combination of the corresponding phantom volume components across the phantom data set (Table I).

The degree of overlap between the observed and model-predicted ablations was quantified by the Jaccard similarity coefficient and used to define the objective function in the optimization. First, binary masks representing the true and model-predicted ablation zones were generated. Given these masked images, the number of pixels in the model-predicted ablation zone overlapping with the observed ablation zone (N_{TP}), the number of voxels in the model-predicted ablation zone which did not overlap with the observed ablation zone (N_{FP}), and the number of voxels in the observed ablation zone which did not overlap with the model-predicted ablation zone (N_{FN}) were used to calculate the similarity metric:

$$\text{Jaccard} = \frac{N_{TP}}{N_{TP} + N_{FP} + N_{FN}} \tag{9}$$

The Jaccard similarity metric ranges from 0 (no overlap) to 1 (perfect match). Therefore, the objective function for the optimization was as follows:

$$\Omega = 1 - \text{Jaccard} \tag{10}$$

The Nelder-Mead downhill simplex algorithm was used to optimize the parameter set for each phantom based on the minimization of the objective function in Eq. (10) [50], [54]. The algorithm uses a direct search method to solve multidimensional unconstrained problems without requiring derivative information. Therefore, the approach can handle non-smooth or noisy objective functions but can take many iterations to converge. The search algorithm was employed until a minimum first-order optimality measure of 0.01 was reached.

I. Phantom Property Model Study

The goal of the above validation study was to validate that the inverse modeling strategy coupled to quantitative ablative

TABLE II
JACCARD SIMILARITY COEFFICIENTS REPRESENTING THE OVERLAP BETWEEN THE OBSERVED AND MODEL-PREDICTED ABLATION ZONES AND ROOT MEAN SQUARE TEMPERATURE ERROR FOR EACH EXPERIMENTAL CASE

	Agar-albumin Phantom	
Case	Jaccard similarity coefficient (%)	Root-mean-square temperature error (°C)
A	95.1	4.1
B	90.9	4.8
C	96.1	4.2
D	90.6	4.3
E	93.5	5.8
F	94.3	5.6
Average	93.4 ± 2.2	4.8

TABLE III
OPTIMIZED ELECTRICAL AND THERMAL CONDUCTIVITIES FOR EACH EXPERIMENTAL CASE OF THE BASE AGAR-ALBUMIN PHANTOM IN THE MODEL VALIDATION STUDY

	Agar-albumin Phantom	
Case	Electrical conductivity (σ)	Thermal conductivity (κ)
A	0.57	0.67
B	0.44	0.34
C	0.58	0.62
D	0.58	0.67
E	0.54	0.47
F	0.50	0.62
Average	0.53 ± 0.05	0.56 ± 0.13

data could be used to estimate material properties. Next, the objective of the phantom material property model study was to use that methodology to develop a functional model relating quantitative MR imaging to ablation modeling parameters (i.e., phantom material properties). To accomplish this, a model of phantom material properties as a function of phantom fat content (measured by the quantitative MR fat imaging protocol described in Section II.C) was constructed using the previously described inverse modeling strategy (II.H).

Next, a leave-one-out cross validation study was performed to characterize this model of phantom material properties as a function of MR-measured fat content. This was achieved by holding out one phantom experiment from the 15 agar-albumin phantoms of varying fat content and using optimized property values from the remaining 14 phantoms to create a linear regression model. The held-out data was then prospectively evaluated to quantify predictive accuracy. Cycling through each data set as a target provides a measure of the predictive capability of the image data-driven material property model. As before, the model-predictive accuracy was calculated using the Jaccard similarity metric Eq. (9); however, no temperature data was recorded during these procedures.

III. RESULTS

A. Model Validation Study

The model validation study evaluated the accuracy of our model in a series of homogenous agar-albumin phantoms by comparing model-predicted results to co-recorded ablation thermal history data. For each phantom, the electrical and thermal conductivities were reconstructed to best fit the model-predicted and observed final ablation zone extents. Temperature maps representing the model-predicted heat distribution for each of the 6 phantoms are presented in Fig. 3. Contours defining the observed and model-predicted final ablation zone extents are included as black and dashed red lines respectively. The degree of volumetric similarity between the ground-truth observed and model-predicted ablation zone extent are presented in Table II as the Jaccard similarity coefficient (averaging 93.4 ± 2.2%). The average observed transverse and axial dimensions attained from mock gross pathology following ablation were 18.2 ± 1.4 mm and 31.0 ± 1.2 mm respectively. Modeled ablation zone diameters differed from observed diameters by 3.3% on average while lengths differed by an average of 3.5%. Furthermore, Table III presents the reconstructed electrical and thermal conductivities found to optimize the predicted ablation zone in each phantom procedure.

For this study, thermal history data were recorded at discrete locations within each phantom throughout ablation. Fig. 4 presents the thermal observations for each temperature sensor in each phantom in the study compared to the model-predicted temperatures at those locations presented as markers and lines respectively. These data serve as a true bystander for validation as they did not contribute to the property reconstruction. Each graph in Fig. 4.A-F corresponds with the ablation extent presented in Fig. 3.A-F. Across the 6 phantom cases, thermal sensors 1 and 3 averaged 12 ± 6 mm and sensors 2 and 4 averaged 30 ± 5 mm vertically above the ablation antenna tip respectively (see arrangement in Fig. 1 for reference). We note that this variation in temperature sensor location across cases makes it such that the observed thermal profiles for a sensor cannot be directly compared across the set of cases. The average root-mean-square (RMS) error with respect to the observed and model-predicted temperatures for each phantom are presented in Table II (averaging 4.8 °C).

B. Phantom Property Model Study

The optimized and property-model-predicted values of electrical and thermal conductivity for the set of 15 agar-albumin-fat phantoms are presented as orange and blue markers respectively in Fig. 5. The orange dashed line represents a linear fit to the full set of 15 optimized properties as a function of measured fat content. The values of electrical ($p > .05$, $r = -.32$) and thermal conductivity ($p < .05$, $r = -.76$) were found to decrease with fat content at rates of 0.74% and 2.61% respectively.

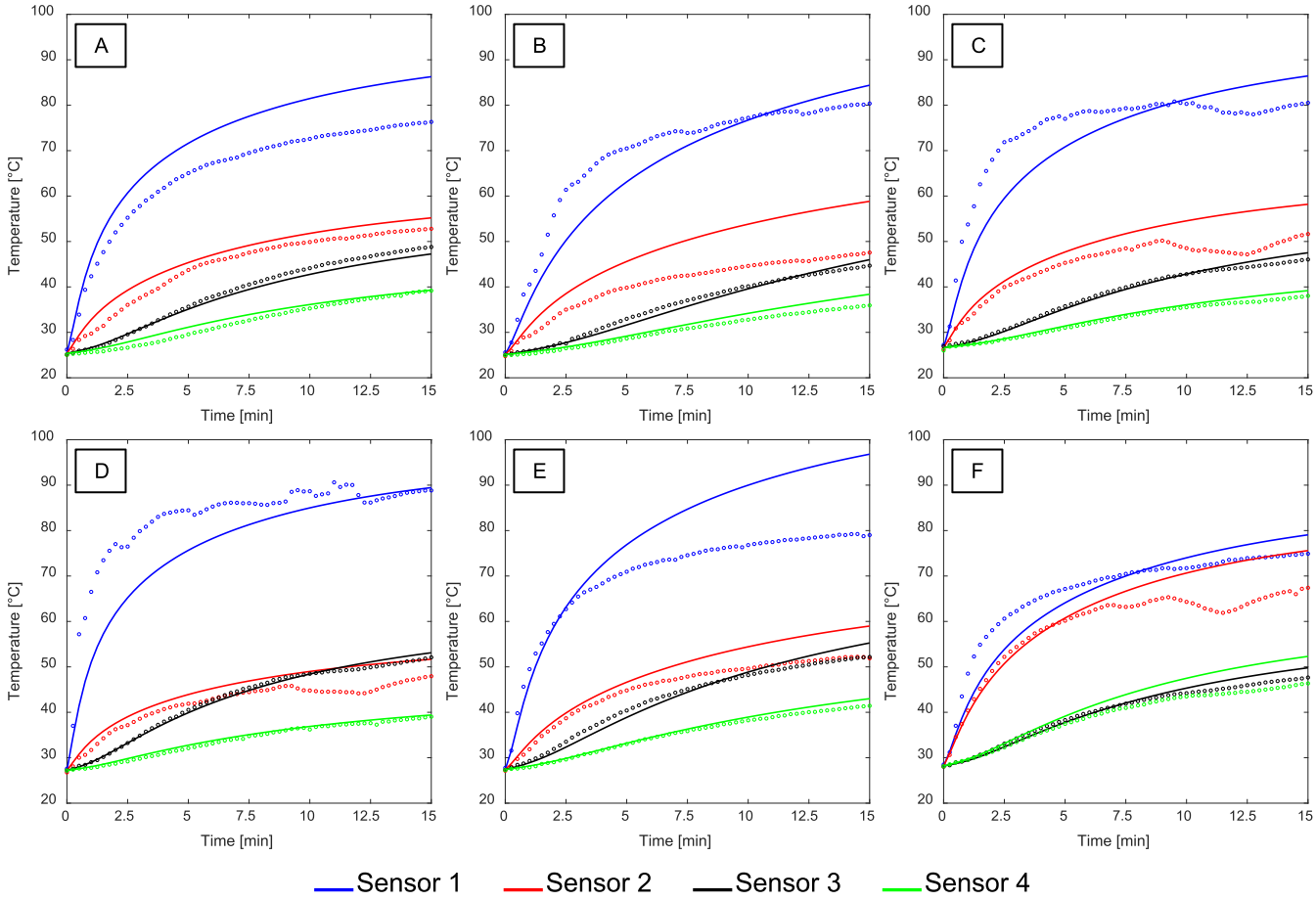

Fig. 4. Observed and model-predicted temperatures as a function of time for each case (A–F) of the base agar-albumin phantom which correspond to the ablation zones presented in Fig. 3. Observed temperatures at the four sensor locations are represented by markers while model-predicted temperatures are represented by solid lines of corresponding color. Note that, due to variability in the placement of thermal sensors, thermal profiles cannot be directly compared across cases.

Fig. 6 presents the percentage overlap between the modeled and observed ablation zones for the 15 agar-albumin-fat phantoms evaluated within the leave-one-out cross validation study represented by a box and whisker chart of the distributions of the Jaccard similarity coefficient. Results are presented for using the optimized property values for each case in orange (averaging 90.2 $\pm$ 3.8%), the predicted property values from the leave-one-out cross validation in blue (averaging 86.6 $\pm$ 5.3%), and estimated property values based on the phantom component volume fractions (i.e., Table I) in grey (averaging 69.3 $\pm$ 9.7%).

IV. Discussion

Based on the work presented in this study and in current literature, tissue thermal and electrical properties are important factors in the development of therapeutic ablation zones and therefore play an important role in the accuracy of predictive MWA procedural modeling [20]–[27]. It is also equally apparent that these tissue properties can vary between patients and can be impacted by disease state [33]–[36]. To date, such variations in tissue properties as a function of patient-specific conditions have been excluded from approaches for predictive modeling of thermal ablative procedures and other current state-of-the-art therapeutic applications [13]–[25]. With this study, we presented two objectives: (1) we developed an inverse modeling approach for estimating phantom thermal and electrical properties from post-procedural ablation extent data and (2) we then used that property estimation approach to develop a phantom property model that was then prospectively employed to estimate phantom properties based on quantitative medical imaging of phantom fat content.

A. Model Validation Study

The objective of this model validation study was to introduce and validate the inverse modeling approach for phantom material property estimation from post-procedural ablation extent data. For this study, a series of 6 identical agar-albumin phantoms with no added fat content were created and ablated. Ablation zone overlap measurements reported in Table II and visually presented in Fig. 3 indicate a strong volumetric agreement between the observed and model-predicted ablation zones (averaging 93.4 $\pm$ 2.2%). These results show that the inverse modeling framework was able to provide accurate prediction of the margins achieved during ablation by estimating phantom

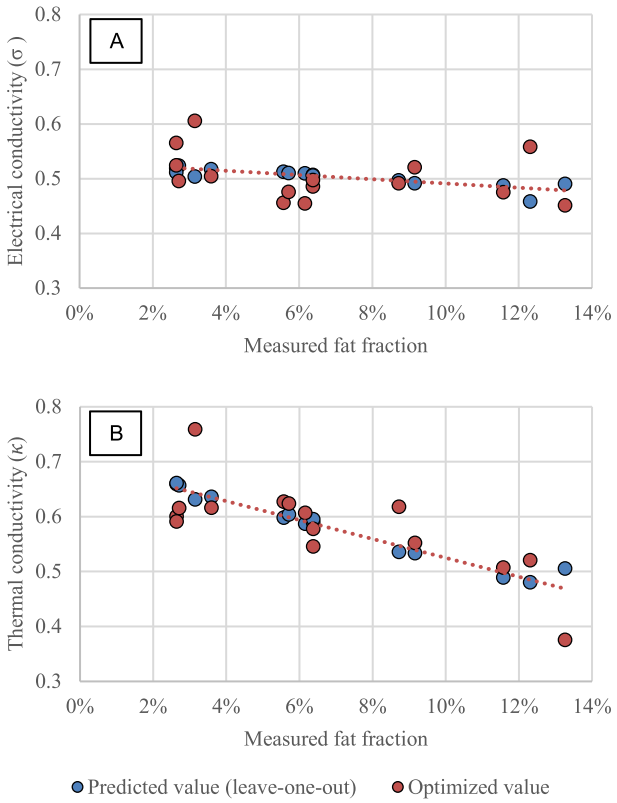

Fig. 5. Determined values of electrical conductivity (A) and thermal conductivity (B) as a function of the MRI-measured fat fraction for each of the 15 agar-albumin-fat phantom cases. The optimized value for a given case is represented by an orange marker. While the predicted value for each case from the leave-one-out evaluation is presented in blue. The orange dashed line represents a linear fit to the optimized values.

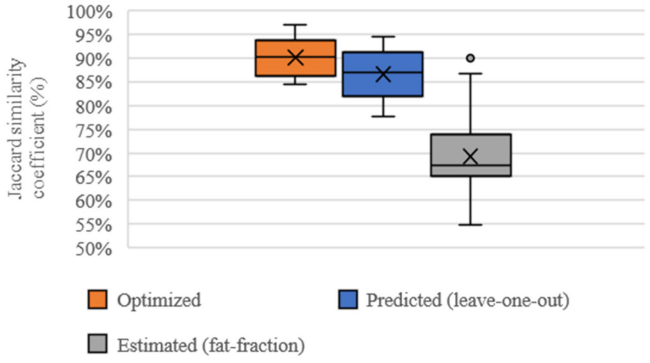

Fig. 6. Percentage overlap between modeled and observed ablation zones for the 15 agar-albumin-fat phantom cases as represented by the Jaccard similarity coefficient. Results using the optimized (orange), leave-one-out predicted (blue), and fat-fraction estimated (grey) are presented. The box and whiskers represent the mean, median, upper and lower quartiles, maximum, and minimum Jaccard similarity coefficient from each modeling approach across the sample of 15 cases.

material property values for the baseline phantom (i.e., no added fat). Further, as the maximization of the ablation zone overlap was employed as the objective function to the inverse model optimization, it is satisfying to observe a good model-data fit.

Results presented in Fig. 4 and Table II illustrate the correspondence between the observed and model-predicted temperatures at each of 4 temperature sensors embedded within the same 6 baseline agar-albumin phantoms (average RMS error of 4.8 °C across all sensors, phantoms, and time points). These temperature data serve as a purely bystander observation (i.e., not utilized within the model optimization) and therefore serve as an independent indication of overall model accuracy, accompanying the volumetric results in Table II and Fig. 3. When comparing these results with similar models of 915 MHz (60 W, 15 min) ablations presented in Deshazer *et al.* 2017 [20], we note that our maximum errors are similar in magnitude. Of note, the thermal profiles presented in [20] more consistently reproduce the first 1–2 minutes of the ablation procedure before reaching much larger error at later time points. This is particularly apparent for temperatures recorded near the ablation source where electromagnetic energy deposition is the primary source of heating. We observe this same phenomenon in 2 of 6 cases (Fig. 4.A and 4.E). However, in Fig. 4.B-D and 4.F, our model underestimates temperatures in the first 1–2 minutes before correcting at the later time points. These results suggest that, while the property reconstruction is leading to accurate prediction of the final ablation volume, the reconstruction of electrical conductivity (σ) within our inverse framework may not be wholly accurate. When contrasting these results to the farther temperature probes (Fig. 4, sensors 2–4) where thermal transfer is the dominant source of heating, we observe much more consistent agreement between model and observation.

B. Phantom Property Model Study

The purpose of this phantom property model study was to evaluate a material property model where phantom properties were estimated based on quantitative medical imaging of phantom fat content using a leave-one-out cross validation approach. For this experiment, 15 phantoms were created with varying fat content. Phantom fat content was then imaged in MRI and phantoms were ablated. Material properties for each of the 15 cases were determined using the property estimation framework outlined in the model validation study (II.H) and are represented by the orange markers in Fig. 5. The average ablation zone volumetric overlap following property optimization (90.2 $\pm$ 3.8%) was in accordance with the results presented in the model validation study. The leave-one-out cross validation evaluation of the property model resulted in ablation zone overlap of an average 86.6 $\pm$ 5.3%. The estimated properties for each case in this evaluation are represented by blue markers in Fig. 5. For further comparison, properties were also estimated for each case based on a linear combination of the component volume fractions of each phantom (i.e., agar gel, albumin, and fat as presented in Table I). The results of the leave-one-out evaluation represent a 17.3% increase in ablation zone overlap when compared to the component volume fraction estimation of properties as seen in Fig. 6.

Based on the phantom component volume fractions, it is expected that both the electrical and thermal conductivity would decrease with the addition of fat to the phantom. This

expectation was realized by the property reconstructions from our inverse model solutions (Fig. 5) which were used to construct the phantom property model. However, only the thermal conductivity was found to have a statistically significant relationship with fat content. Additionally, using linear regression, the ablation zone areas (from mock gross pathology) of the agar-albumin-fat phantoms were found to significantly increase with fat content ($p < .05$, $r = .86$). These results clearly demonstrate that the addition of fat altered the behavior of the phantom and resulted in varying ablation outcome. When considering the clinical application of these results, this could have considerable impact. As an example, when one considers the links between NAFLD, NASH, and hepatocellular carcinoma, the likelihood of patient-specific variability in material properties is high and adds credence to the proposed material property model framework [33]–[35]. It is important to realize that this is just one interesting parameter that could have impact on the clinical presentation of liver cancers (primary and metastatic) within the context of fatty liver disease. There are clearly more possibilities within the battery of imaging with MR but the analysis provided is suggestive. Lastly, while this work has relied on the utilization of an agar-albumin-fat phantom as a surrogate for human liver tissue, both the observed ablation zone dimensions and the reconstructed properties [33] are within the range that have been observed in tissue and do provide some added credence to the experiences reported herein.

C. Limitations

We acknowledge that this early work was conducted with certain assumptions and limitations in both the modeling and testing environments. Regarding material property estimation, in total 5 material properties (ρ, ε, c, σ, and κ) are important to the governing equations of the model (Eq. (1)–(3)). Heat conduction and electromagnetic energy deposition terms are the major contributing factors to the thermal solution of the model. These terms are directly scaled by the thermal (κ) and electrical (σ) conductivities respectively (i.e., the two properties reconstructed within our model). Within this work, we assume that density (ρ), relative permittivity (ε), and specific heat (c) remain constant with changes in fat content. However, based on the errors observed in the model temperature predictions, it is clear that a different approach to the electromagnetic problem should be explored in future iterations of this work (e.g., reconstructing complex permittivity, which is more directly influential to the formation of the electric field). Additionally, a significant amount of work in this field has focused on implementing temperature-dependent material properties within ablation modeling [20]–[25]; whereas we evaluate steady-state properties in this work. As such, the property reconstruction framework presented herein could be further expanded to estimate nonlinear temperature-dependent material properties. In addition, this work did not seek a separate independent testing framework for an independent verification of thermal and dielectric properties. In some respects, the purpose of the paper was to demonstrate the predictive ablation ability of calibrated properties based on a tissue surrogate. With that said, the values determined in the optimization process are in principle a form of property fitting, albeit more challenging than the controlled specimens with standardized testing equipment. Additionally, we acknowledge that our phantom designed to recapitulate tissue behavior used existing data in the literature for the purposes of being a comparator and is a limitation [55].

The phantom testing environment utilized throughout this work was specifically chosen to allow for precise control over phantom fat content. However, tissue perfusion, vascularization, and heterogeneity are likely important factors to ablation zone formation in vivo and will need to be established within our model and testing environment moving forward. It is also important that we identify the challenges to clinical workflow that are introduced by this predictive modeling framework. To establish the proposed property model, a significant series of clinical data would be required with non-standard-of-care preoperative quantitative imaging, with quantitative fat imaging as only one in this case. However, there is precedence for additional required imaging for diagnostic purposes and we suggest that the results of this study are persuasive for the approach as well as point to potential further medical imaging efforts that could lead to better model predictions of ablative therapy.

V. Conclusion

The objective of this work was to develop and experimentally validate a predictive numerical model of microwave ablation procedures with the 915 MHz Perseon ST antenna where patient-specific tissue properties are estimated based on preoperative quantitative MR fat imaging. Procedures were performed in an agar-albumin-fat phantom and were validated with experimental ablation zone and temperature data. While further work is necessary to apply this method to clinical MWA treatment planning, the image data-driven property model approach provided herein is an advancement toward patient-specific predictive modeling of MWA procedures.

References

[1] U. Leung *et al.*, "Long-term outcomes following microwave ablation for liver malignancies," *Brit. J. Surg.*, vol. 102, pp. 85–91, 2015.
[2] E. S. Alexander *et al.*, "Microwave ablation of focal hepatic malignancies regardless of size: A 9-year retrospective study of 64 patients," *Eur. J. Radiol.*, vol. 84, no. 6, pp. 1083–1090, 2015.
[3] R. C. G. Martin, C. R. Scoggins, and K. M. McMasters, "Safety and efficacy of microwave ablation of hepatic tumors: A prospective review of a 5-year experience," *Ann. Surg. Oncol.*, vol. 17, pp. 171–178, 2010.
[4] C. Simon, D. E. Dupuy, and W. W. Mayo-Smith, "Microwave ablation: Principles and applications," *Radiographics*, vol. 25, pp. S69–S83, 2005.
[5] C. Correa-Gallego *et al.*, "A retrospective comparison of microwave ablation vs. radiofrequency ablation for colorectal cancer hepatic metastases," *Ann. Surg. Oncol.*, vol. 21, no. 13, pp. 4278–4283, 2014.
[6] T. A. Potretzke *et al.*, "Microwave versus radiofrequency ablation treatment for hepatocellular carcinoma: A comparison of efficacy at a single center," *J. Vascular Intervention Radiol.*, vol. 27, no. 5, pp. 631–638, 2016.
[7] S. Pathak *et al.*, "Ablative therapies for colorectal liver metastases: A systematic review," *Colorectal Dis.*, vol. 13, no. 9, pp. e252–e265, 2011.
[8] M. A. Lewis, R. M. Staruch, and R. Chopra, "Thermometry and ablation monitoring with ultrasound," *Int. J. Hyperthermia*, vol. 31, no. 2, pp. 163–181, 2015.
[9] B. D. De Senneville *et al.*, "MR thermometry for monitoring tumor ablation," *Eur. Radiol.*, vol. 17, no. 9, pp. 2401–2410, 2007.

[10] P. Prakash, "Theoretical modeling for hepatic microwave ablation," *Open Biomed. Eng. J.*, vol. 4, pp. 27–38, 2010.

[11] R. S. Winokur *et al.*, "Characterization of in vivo ablation zones following percutaneous microwave ablation of the liver with two commercially available devices: Are manufacturer published reference values useful?" *J. Vascular Intervention Radiol.*, vol. 25, no. 12, pp. 1939–1946, 2014.

[12] D. T. Glidden *et al.*, "Clinically observed ablation volumes as compared to vendor specified volumes: The emperor's new clothes," *J. Vascular Intervention Radiol.*, vol. 25, no. 3, 2014, Art. no. S76.

[13] C. L. Brace, "Dual-slot antennas for microwave tissue heating: Parametric design analysis and experimental validation," *Med. Phys.*, vol. 38, pp. 4232–4240, 2011.

[14] C. L. Brace *et al.*, "Microwave ablation with a triaxial antenna: Results in ex vivo bovine liver," *IEEE Trans. Microw. Theory Techn.*, vol. 53, no. 1, pp. 215–220, Jan. 2005.

[15] Y. Liu *et al.*, "Phantom experimental study on microwave ablation with a water-cooled antenna," *Int. J. Hyperthermia*, vol. 23, no. 4, pp. 381–386, 2007.

[16] P. Prakash *et al.*, "Design optimization of a robust sleeve antenna for hepatic microwave ablation," *Phys. Med. Biol.*, vol. 53, no. 4, pp. 1057–1069, 2008.

[17] S. Etoz and C. L. Brace, "Analysis of microwave ablation antenna optimization techniques," *Int. J. RF Microw. Comput.-Aided Eng.*, vol. 28, 2018, Art. no. e21224.

[18] W. Zhai *et al.*, "Preoperative surgery planning for percutaneous hepatic microwave ablation," in *Proc. Int. Conf. Med. Image Comput. Comput.-Assisted Intervention*, 2008, pp. 569–577.

[19] J. A. Collins *et al.*, "Method for evaluation of predictive models of microwave ablation via post-procedural clinical imaging," *Proc. SPIE*, vol. 9415, 2015, Art. no 94152F.

[20] G. Deshazer *et al.*, "Computational modelling of 915 MHz microwave ablation: Comparative assessment of temperature-dependent tissue dielectric models," *Med. Phys.*, vol. 44, no. 9, pp. 4859–4868, 2017.

[21] Z. Ji and C. L. Brace, "Expanded modelling of temperature-dependent dielectric properties for microwave thermal ablation," *Phys. Med. Biol.*, vol. 56, no. 16, pp. 5249–5264, 2011.

[22] D. Liu and C. L. Brace, "Numerical simulation of microwave ablation incorporating tissue contraction based on thermal dose," *Phys. Med. Biol.*, vol. 62, no. 6, pp. 2070–2086, 2017.

[23] V. Lopresto, R. Pinto, and M. Cavagnaro, "Experimental characterization of the thermal lesion induced by microwave ablation," *Int. J. Hyperthermia*, vol. 30, no. 2, pp. 110–118, 2013.

[24] V. Lopresto *et al.*, "Treatment planning in microwave thermal ablation: Clinical gaps and recent research advances," *Int. J. Hyperthermia*, vol. 33, no. 1, pp. 83–100, 2016.

[25] M. Cavagnaro, R. Pinto, and V. Lopresto, "Numerical models to evaluate the temperature increase induced by ex vivo microwave thermal ablation," *Phys. Med. Biol.*, vol. 60, no. 8, pp. 3287–3311, 2015.

[26] V. Lopresto *et al.*, "Microwave thermal ablation: Effects of tissue properties variations on predictive models for treatment planning," *Med. Eng. Phys.*, vol. 46, pp. 63–70, 2017.

[27] J. Sebek *et al.*, "Sensitivity of microwave ablation models to tissue biophysical properties: A first step toward probabilistic modelling and treatment planning," *Med. Phys.*, vol. 43, no. 5, pp. 2649–2661, 2016.

[28] C. Rossmann and D. Haemmerich, "Review of temperature dependence of thermal properties, dielectric properties, and perfusion of biological tissues at hyperthermic and ablation temperatures," *Critical Rev. Biomed. Eng.*, vol. 42, no. 6, pp. 467–492, 2014.

[29] D. Yang *et al.*, "Measurement and analysis of tissue temperature during microwave liver ablation," *IEEE Trans. Biomed. Eng.*, vol. 54, no. 1, pp. 150–155, Jan. 2006.

[30] D. Haemmerich *et al.*, "Hepatic bipolar radiofrequency ablation creates coagulation zones close to blood vessels: A finite element study," *Med. Biol. Eng. Comput.*, vol. 41, no. 3, pp. 317–323, 2003.

[31] W. Schramm, D. Yang, and D. Haemmerich, "Contribution of direct heating, thermal conduction and perfusion during radiofrequency and microwave ablation," in *Proc. Annu. Int. Conf. Proc. IEEE Eng. Med. Biol. Soc.*, 2006, pp. 5013–5016.

[32] N. C. Yu *et al.*, "Microwave liver ablation: Influence of hepatic vein size on heat-sink effect in a porcine model," *J. Vascular Intervention Radiol.*, vol. 19, no. 7, pp. 1087–1092, 2008.

[33] A. Marengo, C. Rosso, and E. Bugianesi, "Liver cancer: Connections with obesity, fatty liver, and cirrhosis," *Annu. Rev. Med.*, vol. 67, pp. 103–117, 2016.

[34] A. P. O'Rourke *et al.*, "Dielectric properties of human normal, malignant and cirrhotic liver tissue: In vivo and ex vivo measurements from 0.5 to 20 GHz using a precision open-ended coaxial probe," *Phys. Med. Biol.*, vol. 52, no. 15, pp. 4707–4719, 2007.

[35] A. Peyman *et al.*, "Variation in dielectric properties due to pathological changes in human liver," *Bioelectromagnetics*, vol. 36, no. 8, pp. 603–612, 2015.

[36] V. Bhat *et al.*, "Quantification of liver fat with mDIXON magnetic resonance imaging, comparison with the computed tomography and the biopsy," *J. Clin. Diagnostic Res.*, vol. 11, no. 7, pp. 6–10, 2017.

[37] P. M. Meaney *et al.*, "Integration of microwave tomography with magnetic resonance for improved breast imaging," *Med. Phys.*, vol. 40, Oct. 2013, Art. no. 103101.

[38] M. A. Kandadai, J. L. Raymond, and G. J. Shaw, "Comparison of electrical conductivities of various brain phantom gels: Developing a brain gel model," *Mater. Sci. Eng. C*, vol. 32, no. 8, pp. 2664–2667, 2012.

[39] B. D. Roebuck and S. A. Goldblith, "Dielectric properties at microwave frequencies of agar gels," *J. Food Sci.*, vol. 40, no. 5, pp. 899–902, 1975.

[40] O. K. Bates, "Thermal conductivity of liquid silicones," *Ind. Eng. Chem.*, vol. 41, no. 9, pp. 1966–1968, 1949.

[41] M. Zhang *et al.*, "Experimental determination of thermal conductivity of water-agar gel at different concentrations and temperatures," *J. Chem. Eng. Data*, vol. 56, no. 4, pp. 859–864, 2011.

[42] J. Corach, P. A. Sorichetti, and S. D. Romano, "Electrical properties of vegetable oils between 20 Hz and 2 MHz," *Int. J. Hydrogen Energy*, vol. 39, no. 16, pp. 8754–8758, 2014.

[43] W. E. Pace, W. B. Westphal, and S. A. Goldblith, "Dielectric properties of commercial cooking oils," *J. Food Sci.*, vol. 33, pp. 30–36, 1968.

[44] Engineering ToolBox, "Specific heat of liquids and fluids," 2003. [Online]. Available: https://engineeringtoolbox.com/specific-heat-fluids-d_151.html

[45] A. Turgut, I. Tavman, and S. Tavman, "Measurement of thermal conductivity of edible oils using transient hot wire method," *Int. J. Food Properties*, vol. 12, no. 4, pp. 741–747, 2009.

[46] J. Wang *et al.*, "Dielectric properties of egg whites and whole eggs as influenced by thermal treatments," *LWT-Food Sci. Technol.*, vol. 42, no. 7, pp. 1204–1212, 2009.

[47] J. S. R. Coimbra *et al.*, "Density, heat capacity and thermal conductivity of liquid egg products," *J. Food Eng.*, vol. 74, no. 2, pp. 186–190, 2006.

[48] LumaSense Technol., Santa Clara, CA, USA. *Luxtron 812 Industrial Temperature Monitor Data Sheet*. (Mar. 2015) [Online]. Available: http://martechcontrols.com/upload_file/EN-Luxtron-812-Industrial.Datasheet.MAR.2015.pdf

[49] Philips, Amsterdam, The Netherlands. *Product Brochure Philips mDIXON Quant MR Clinical Application*. (Nov. 2015) [Online]. Available: https://www.usa.philips.com/healthcare/product/HCNMRB462/

[50] *COMSOL Multiphysics Reference Manual*, COMSOL Inc., Burlington, MA, USA, 2013.

[51] I. A. Chang and U. D. Nguyen, "Thermal modeling of lesion growth with radiofrequency ablation devices," *Biomed. Eng. Online*, vol. 3, 2004, Art. no. 27.

[52] P. R. Amestoy *et al.*, "A fully asynchronous multifrontal solver using distributed dynamic scheduling," *SIAM J. Matrix Anal. A*, vol. 23, pp. 15–41, 2001.

[53] S. J. Fahrenholtz *et al.*, "Theoretical model for laser ablation outcome predictions in brain: Calibration and validation on clinical MR thermometry images," *Int. J. Hyperthermia*, vol. 34, no. 1, pp. 101–111, 2018.

[54] J. C. Lagarias *et al.*, "Convergence properties of the Nelder-Mead simplex method in low dimensions," *SIAM J. Optim.*, vol. 9, pp. 112–147, 1998.

[55] P. A. Hasgall *et al.*, "IT'IS Database for thermal and electromagnetic parameters of biological tissues," Version 4.0, May 2018, doi: 10.13099/VIP21000-04-0.